Journal of
Materials Chemistry A

Accepted Manuscript

This article can be cited before page numbers have been issued, to do this please use: D. Ansovini, C. J. J. Lee, C. S. Chua, J. Ong, H. R. Tan, W. Webb, R. Raja and Y. Lim, *J. Mater. Chem. A*, 2016, DOI: 10.1039/C6TA00540C.

ROYAL SOCIETY OF CHEMISTRY

www.rsc.org/materialsA

View Article Online
DOI: 10.1039/C6TA00540C

Journal of Materials Chemistry A

COMMUNICATION

Highly active hydrogen evolution electrocatalyst based on cobalt-nickel sulfide composite electrode†

Received 00th January 20xx,
Accepted 00th January 20xx

DOI: 10.1039/x0xx00000x

www.rsc.org/

Davide Ansovini,[a,b] Coryl Jing Jun Lee,[a] Chin Sheng Chua,[a] Lay Ting Ong,[a] Hui Ru Tan,[a] William Webb,[b] Robert Raja[b] and Yee-Fun Lim*[a]

A novel Co_9S_8-Ni_xS_y/Ni foam composite material was synthesized through the thermal decomposition of a cobalt-thiourea molecular precursor onto the 3D metallic support. The obtained electrode exhibited good activity toward the hydrogen evolution reaction in alkaline medium, requiring small overpotential of 163 mV at a current density of 10 mA cm^{-2}, which is one of the lowest ever reported among transition metal sulfides materials.

Recent projections have shown that the world population will increase from 7.2 billion in 2015 to between 9.6 billion and 12.3 billion in 2100.[1] Reconciling the energy needs of a large population while mitigating global warming appears to be strickly dependent on renewable energy sources (solar, wind, etc.) and their capacity to be cost-effective and easily scalable for a global and diffuse deployment. One of the principal drawbacks of relying abundantly on renewable energy is represented by its intermittent nature, which does not guarantee a constant electric supply to the grid. In this regard several technologies based on energy storage have been developed, where the energy derived by a renewable source can be stored as thermal,[2] electrochemical,[3] chemical,[4] just to name a few. Among the various existing technologies hydrogen (H_2) production through solar-driven water electrolysis has received considerable attention, given the potential key role of hydrogen as a clean fuel and energy carrier.[5,6]

In order to be commercially viable, electrocatalytic water electrolysis requires active, durable and low-cost electrocatalysts for the hydrogen evolution reaction (HER) and the oxygen evolution reaction (OER). At present, platinum (Pt) and its alloys represent the most efficient catalysts for the HER in both acidic and basic environments, although its high cost and scarcity severely preclude a large-scale use for H_2 production.[7,8] During the past 10 years numerous efforts have been devoted to the identification of active, stable and low-cost HER electrocatalysts able to efficiently work under harsh (acidic and/or basic) and/or neutral electrolytes. Relevant examples include first-row (Co, Ni, Fe)[8–13] and group VI (Mo, W)[14–18] transition metal chalcogenides, nitrides,[19] phosphides,[20–23] group VI transition metal carbides,[24,25] borides[26] and transition metal alloys.[7,27] Particularly, first-row transition metal sulfides such as CoS_2,[8,10,11,9,28] Co_9S_8,[29,30] NiS_2,[28,31] Ni_3S_2,[32] Co-S,[33] Ni-S[12] have recently emerged as a promising class of active HER electrocatalysts, showing to possess good activity over a broad pH range and reasonable chemical stability under electrocatalytic conditions. Although promising, these materials have not been extensively investigated yet, especially in their behaviour under alkaline media. Indeed, it is highly desirable to find new active and stable HER catalysts operating under alkaline conditions, considering that the most active OER catalysts made of earth-abundant elements are either unstable or inactive under acidic medium.[4] They would also be more compatible with existing water electrolysis plants which are usually based on cells with alkaline electrolyte.[34]

Catalyst nanostructuring onto conductive substrates is an effective synthetic strategy for increasing the surface area, which leads to an improvement of the HER electrocatalytic activity.[8,10,11] Moreover, the *in situ* growth of electrocatalytic materials onto binder-free and three-dimensional (3D) substrates plays a crucial role in obtaining composite electrodes with high mechanical stability and strong interface adhesion.[8,11,15] At present, carbon-based substrates have been mainly investigated, such as reduced graphene oxide,[11,18] carbon nanotubes,[11,24] carbon paper[8] and carbon cloth[21] because of their high electronic conductivity, high surface area and inertness. Nickel foam is another substrate of particular interest considering its unique 3D macroporous structure, high electronic conductivity and low cost. Besides, the intrinsic activity of metallic nickel towards the HER under alkaline conditions implies the possibility of designing novel composite electrodes with unprecedented properties.[35] Notable examples of HER electrocatalysts supported onto Ni foam include MoS_2,[15] Ni_3S_2,[32] Ni_5P_4-Ni_2P,[22] Ni-Se nanowires,[36] Mo_2C.[35]

[a] Institute of Materials Research and Engineering (IMRE), A*STAR (Agency for Science, Technology and Research), 2 Fusionopolis Way, Innovis, #08-03, Singapore 138634, Republic of Singapore. *Email: limyf@imre.a-star.edu.sg
[b] School of Chemistry, University of Southampton, Highfield, Southampton SO17 1BJ, United Kingdom.

† Electronic Supplementary Information (ESI) available: See DOI: 10.1039/x0xx00000x

View Article Online
DOI: 10.1039/C6TA00540C

In this work we report a facile synthetic strategy for the fabrication of a multi-phasic cobalt-nickel sulfide HER electrocatalyst supported onto a commercially available Ni foam (Nif). Cobalt and nickel sulfide nanoparticles were generated *in situ* upon thermal pyrolysis of thiourea, due to the formation of reactive sulfurized molecular species that directly react with the metallic atoms. A detailed investigation on the effect of annealing temperature and time was carried out, establishing a structure-property relation through a combined characterization analyses coupled with HER electrocatalytic tests. The optimum electrode showed a small overpotential of 163 mV required to reach a current density of 10 mA/cm^2, a Tafel slope of 88 mV/dec and great long-term stability as long as 72 hours.

Our synthetic strategy was inspired by earlier works reporting the formation of pure cobalt sulfide nanoparticles through the thermal annealing under inert atmosphere of a preformed Co-thiourea molecular complex in methanol.[37,38] In our method the Co-thiourea complex was first adsorbed onto a pre-cleaned Ni foam (Nif) through dip coating, and subsequently annealed under N_2. The metal loading in the electrode can be controlled simply by repeating the two steps of dip coating-annealing (see Experimental details†). We also found that by using only thiourea as a molecular precursor, pure crystalline Ni_3S_2 (heazlewoodite) was formed on the surface of the Nif, whereas in the case of the Co-thiourea precursor, a series of different crystalline phases of nickel sulfides and only one well-defined phase of cobalt sulfide (Co_9S_8) were obtained. Annealing temperature and time were systematically varied (400-500 °C, 10-90 min) for both the monometallic and the bimetallic electrodes, giving precious insights into the structural and morphological transformations involved. Samples obtained by the thermal decomposition of thiourea at a specific temperature (T) and time (t) will be referred as Ni_3S_2/Nif(T,t), whereas those obtained by the thermal decomposition of Co-thiourea complex will be referred as Co_9S_8-Ni_xS_y/Nif(T,t). Unless otherwise stated, all the characterized samples showed below were synthesized by performing 5 cycles of dip coating-annealing.

X-ray diffraction (XRD) patterns for the Ni_3S_2/Nif and the Co_9S_8-Ni_xS_y/Nif electrodes are reported in Fig. S2 and Fig. 1, respectively. In the case of the monometallic system, the XRD patterns show the formation of a pure rhombohedral Ni_3S_2 (JCPDS no. 30-0863) for all the different annealing conditions. No secondary phases were detected. A contrasting behaviour can be observed for the Co_9S_8-Ni_xS_y/Nif electrode, with the formation of a variety of nickel sulfide phases and the cubic Co_9S_8. As we can note from the spectra, the diffraction peaks were carefully indexed by comparing the experimental pattern with reported data, and compounds such as NiS_2 (JCPDS no. 03-0734), $Ni_{17}S_{18}$ (JCPDS no. 76-2306), NiS (JCPDS no. 12-0041), Ni_7S_6 (JCPDS no. 24-1021) and Ni_3S_2 (JCPDS no. 30-0863) were identified. Only one phase of cobalt sulfide was detected, with diffraction peaks indexed to the cubic Co_9S_8 (JCPDS no. 86-2273). Interestingly, the relative presence of each nickel sulfide species depends on the annealing parameters, with sulfur-deficient phases (Ni/S > 1) favoured at high temperature and long annealing time. For instance, the Co_9S_8-Ni_xS_y/Nif(500,90) shows only the presence of Ni_3S_2 (Ni/S = 1.5) along with Co_9S_8, in stark contrast with the multitude of phases observed for the other investigated conditions. The Co_9S_8 phase starts to appear after annealing at 400

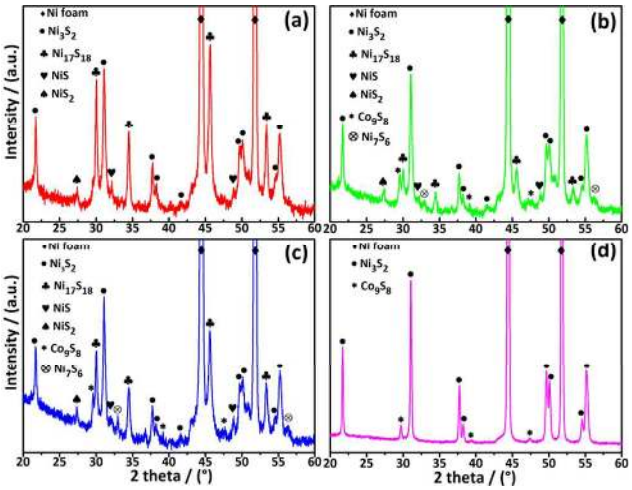

Fig. 1 XRD patterns for Co_9S_8-Ni_xS_y/Nif different annealing temperatures and times (a) 400 °C 10 min, (b) 400°C 90 min; (c) 500°C 10 min, (d) 500°C 90 min.

°C for 90 min (Fig. 1(b)) and its structural nature does not change with varying the annealing parameters. The presence of Co_9S_8 was further confirmed by Raman spectroscopy as highlighted in Fig. S3, where two peaks located at 510 cm^{-1} and 1040 cm^{-1} match well with those reported for the pure Co_9S_8.[39] A broad peak at around 300-350 cm^{-1} lies in the characteristic range of Ni_3S_2,[40] although its poor resolution hinders a defined deconvolution of the peaks documented in the literature. This could be also due to an overlapping with the other nickel sulfide phases which may have a similar Raman pattern.

The SEM images for the Ni_3S_2/Nif (Fig. S4) and Co_9S_8-Ni_xS_y/Nif (Fig. 2) reveal the formation of a nanoparticulate morphology of similar nature for both electrodes. As a common feature these nanoparticles tend to grow and agglomerate with increasing annealing temperature and time. TEM analysis performed on the Co_9S_8-Ni_xS_y/Nif samples shows the presence of small nanoparticles having a mean diameter of less than 20 nm (Fig. 3). Fig. 3(e) and 3(f)

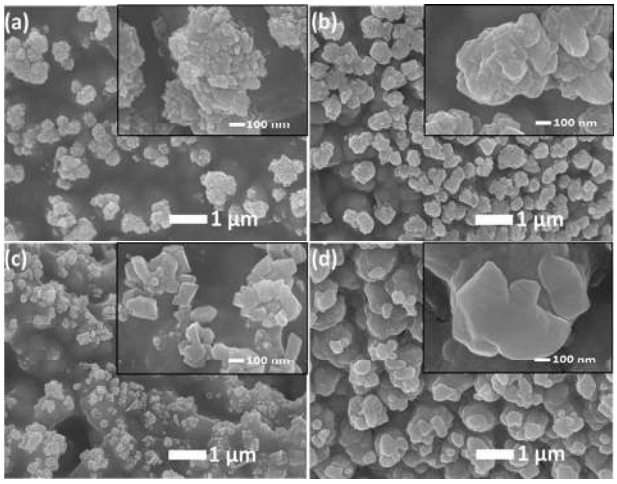

Fig. 2 Low- and high-magnification SEM images for Co_9S_8-Ni_xS_y/Nif at different annealing temperatures and times (a) 400 °C 10 min, (b) 400°C 90 min; (c) 500°C 10 min, (d) 500°C 90 min.

View Article Online
DOI: 10.1039/C6TA00540C

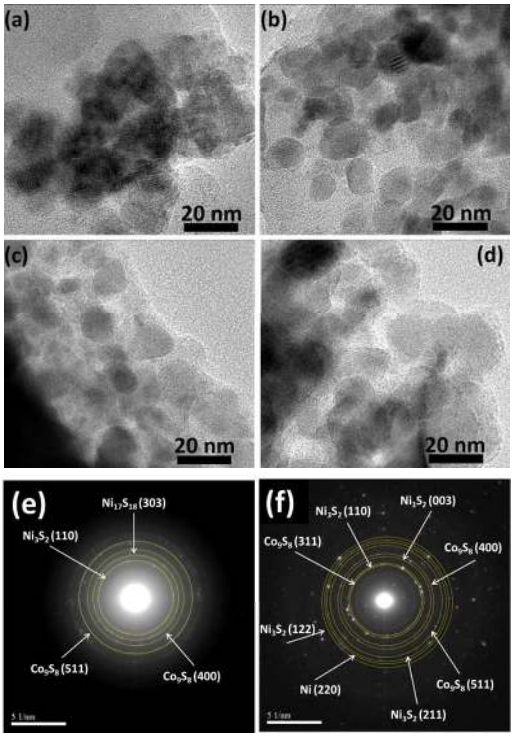

Fig. 3 TEM images for Co_9S_8-Ni_xS_y/Nif at different annealing temperatures and times (a) 400 °C 10 min, (b) 400°C 90 min; (c) 500°C 10 min, (d) 500°C 90 min. Selected area electron diffraction patterns for Co_9S_8-Ni_xS_y/Nif at (e) 500°C 10 min and (f) 500°C 90 min.

display the selected area electron diffraction (SAED) patterns for the Co_9S_8-Ni_xS_y/Nif(500,10) and Co_9S_8-Ni_xS_y/Nif(500,90), respectively, with several bright rings which can be indexed to different lattice planes belonging to Ni_3S_2 and Co_9S_8. However not all the phases identified through XRD can be traced in the SAED patterns, given the small proximity of the diffracted peaks and the intrinsic low angular resolution of the electron diffraction technique.

The atomic percentage of cobalt was determined using energy-dispersive X-ray spectroscopy (EDX) and it was around 4% for all the different electrodes as reported in Fig. S5. A semi-quantitative estimate of the mass loading can be calculated for the Co_9S_8-Ni_xS_y/Nif, giving a value of roughly 2 mg/cm^2 for Co_9S_8 and 7 mg/cm^2 for Ni_xS_y (assuming Ni/S = 1.5). In the case of the monometallic Ni_3S_2/Nif electrode, a similar mass loading of 7 mg/cm^2 was obtained (see Fig. S6 for the EDX spectra). Significant amount of carbon and nitrogen was detected as a result of the formation of carbonaceous side products originating from the pyrolitic decomposition of thiourea.[41]

X-ray electron photoelectron spectroscopy (XPS) was performed in order to analyze the chemical composition of the samples and the oxidation state of the elements. The Ni2p, Co2p and S2p XPS spectra of the Co_9S_8-Ni_xS_y/Nif materials are reported in Fig. S7, S8, and S9, respectively. The Ni2p patterns show the presence of a mixed Ni^0/Ni^{2+} oxidation states for the Co_9S_8-Ni_xS_y/Nif(400,10) and Co_9S_8-Ni_xS_y/Nif(500,90), with the typical binding energy of 853.0 eV for Ni^0 and 856.0 eV for Ni^{2+}. These values fit well with previous XPS spectra of pure Ni_3S_2,[42] which is a compound with a rich redox chemistry, possessing Ni^0, Ni^{1+} and Ni^{2+} species. As suggested by Buckely *et al.*, the Ni2p$_{3/2}$ peak at 856.0 eV can be attributed to the presence of $Ni(OH)_2$ formed on the surface of the Ni_3S_2 upon exposure to atmospheric air.[43] This peak is consistently present for all the samples, regardless of the adopted annealing condition. The Co_9S_8-Ni_xS_y/Nif(400,90) and Co_9S_8-Ni_xS_y/Nif(500,10) materials show a slightly different chemistry, with the occurrence of Ni^{2+} species (853.7 eV) derived from nickel sulfide[44] and no peaks related to Ni^0. The Co2p XPS spectra reveal the presence of Co^{2+} species for all the samples, with a binding energy of 781.0-782.0 eV (Co2p$_{3/2}$), characteristic of Co_9S_8.[29] Co^{3+} species was detected only for the Co_9S_8-Ni_xS_y/Nif(500,90), with the Co2p$_{3/2}$ peak located at 778.4 eV. This may be due to the partial oxidation of the Co^{2+} to Co^{3+} on the surface resulting from the prolonged annealing under relatively high temperature. The S2p XPS spectra are in agreement with the typical binding energies for nickel and cobalt sulfides, with the S2p$_{3/2}$ peak located at 161.4-162.4 eV attributed to a S^{-2} oxidation state bonded to the metal cation.[29,42] In all the samples it is possible to identify another S2p$_{3/2}$ peak at 168.0-169.0 eV, which is linked to the presence of SO_3^{-2}/SO_4^{-2} species on the surface of the metal sulfides resulting from the exposure to air.[43] A detailed quantitatve analysis of the XPS derived from the fitting of the experimental spectra can be found in Table S1. The results show that the Co/Ni atomic ratio is 1.2, 1.0, 0.5 and 3.3 for the Co_9S_8-Ni_xS_y/Nif(400,10), Co_9S_8-Ni_xS_y/Nif(400,90), Co_9S_8-Ni_xS_y/Nif(500,10) and Co_9S_8-Ni_xS_y/Nif(500,90), respectively. Furthermore, the S/(Co+Ni) ratio is lower for the electrodes treated at 500°C, which is in line with the structural modifications observed by XRD, with sulfur-poor nickel sulfide phases favoured at high temperature. The Ni2p and S2p XPS spectra of the monometallic Ni_3S_2/Nif electrode displayed in Fig. S10 fit with the patterns reported in the literature for pure Ni_3S_2.[42]

The HER activity of the Co_9S_8-Ni_xS_y/Nif and Ni_3S_2/Nif electrodes was evaluated through linear sweep voltammetry in 1M KOH aqueous electrolyte and the correspondent polarization curves after iR correction are displayed in Fig. 4(a) and (b), respectively. As we can observe in Table 1, the HER activity of the Co_9S_8-Ni_xS_y/Nif is superior compared to the monometallic Ni_3S_2/Nif electrode. The Co_9S_8-Ni_xS_y/Nif(500,10) electrode showed the best performance with a required small overpotential of 163 mV to reach a current density of 10 mA/cm^2, typical figure of merit used for comparing the activity of electrocatalysts in a hypotetical solar-driven electrochemical water splitting device operating at 12.3% efficiency.[45] This value compares well with the best reported earth-abundant metal HER electrocatalysts under alkaline media, and a quantitative comparison in terms of HER performance can be found in Table S2. For the Co_9S_8-Ni_xS_y/Nif sample, the HER activity trend is correlated with the specific annealing conditions. The Co_9S_8-Ni_xS_y/Nif(500,90) electrode showed a dramatic drop in activity compared to the other ones, with an overall performance even worse than the bare Ni foam. This difference can also be seen in the value of the Tafel slopes, which is an indication of the mechanistic reaction pathway. Similar values ranging from 83 to 91 mV/dec were found for the active Co_9S_8-Ni_xS_y/Nif(400,10), Co_9S_8-Ni_xS_y/Nif(400,90) and Co_9S_8-Ni_xS_y/Nif(500,10), suggesting a mixed Volmer-Heyrovsky rate-determining step (RDS) occurring on these electrodes. In stark contrast, the Tafel slope of the Co_9S_8-Ni_xS_y/Nif(500,90) electrode is 117 mV/dec, quite close to the value

View Article Online
DOI: 10.1039/C6TA00540C

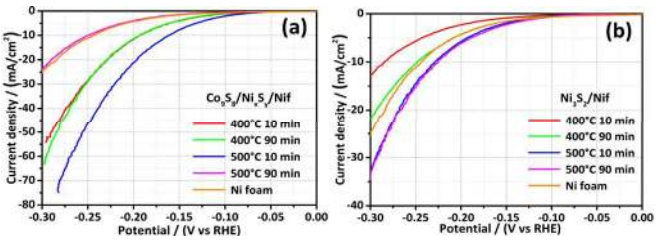

Fig. 4 iR-corrected polarization curves for (a) Co_9S_8-Ni_xS_y/Nif and (b) Ni_3S_2/Nif at different annealing temperatures and times in 1M KOH electrolyte.

Sample	Annealing condition	η (1 mA/cm²) (mV)	η (10 mA/cm²) (mV)	Tafel slope (mV/dec)	C_{dl} (mF/cm²)	R_{ct} (Ω)
Co_9S_8-Ni_xS_y/Nif	400°C 10 min	95	193	91	58.9	3.5
Co_9S_8-Ni_xS_y/Nif	400°C 90 min	100	193	83	43.7	3.6
Co_9S_8-Ni_xS_y/Nif	500°C 10 min	79	163	88	63.8	2.9
Co_9S_8-Ni_xS_y/Nif	500°C 90 min	135	252	117	17.4	4.2
Ni_3S_2/Nif	400°C 10 min	157	284	106	10.3	23.0
Ni_3S_2/Nif	400°C 90 min	130	248	98	8.1	7.8
Ni_3S_2/Nif	500°C 10 min	122	230	87	12.9	4.8
Ni_3S_2/Nif	500°C 90 min	116	225	93	15.6	4.8
Bare Nif		128	245	126	$3.8 \cdot 10^{-4}$	9.3

Table 1 Summary of the electrochemical properties of the Co_9S_8-Ni_xS_y/Nif and Ni_3S_2/Nif electrodes for the HER in 1M KOH.

obtained for the bare Ni foam, typical of a pure Volmer RDS. The much lower activity of the Co_9S_8-Ni_xS_y/Nif(500,90) sample can be ascribed to the different structural, compositional and morphological properties. In particular, three factors appear to be significantly different from the more active bimetallic electrodes: i) higher Co/Ni superficial atomic ratio, ii) absence of other nickel sulfides phases apart from Ni_3S_2, iii) nanoparticulate agglomeration. A higher Co/Ni atomic ratio means that more Co_9S_8 particles are exposed to the electrolyte compared to Ni_3S_2, and this can explain the mechanistic difference existing for the Co_9S_8-Ni_xS_y/Nif(500,90). Indeed, the Tafel slopes of the monometallic Ni_3S_2/Nif lie in the range 87-106 mV/dec (Table 1), similar to the values obtained for the Co_9S_8-Ni_xS_y/Nif(400,10), Co_9S_8-Ni_xS_y/Nif(400,90) and Co_9S_8-Ni_xS_y/Nif(500,10) materials. This suggests that Ni_3S_2 plays an active role in the mechanistic pathway of the HER, perhaps having a more favourable adsorption capacity of water molecules compared to Co_9S_8. Recently, Feng *et al*. showed a rather poor HER activity of Co_9S_8 in alkaline media, with a required overpotential of 250 mV to reach a current density of 10 mA/cm^2.[30] This value is in agreement with the performance of the Co_9S_8-Ni_xS_y/Nif(500,90), leading to the conclusion that pure Co_9S_8 is not a particularly active catalyst for the HER. However it is worth noting that even the pure Ni_3S_2/Nif has a much lower activity compared to the active bimetallic electrodes. The best material showed a modest overpotential of 225 mV in order to reach 10 mA/cm^2, only 20 mV lower than the bare Ni foam. In this regard, we propose the presence of a synergistic effect between Co_9S_8 and Ni_3S_2 as the main reason why we observe a dramatic improvement in the HER activity of the Co_9S_8-Ni_xS_y/Nif under well-defined synthetic conditions. This effect arises from an intimate contact of the two phases and an appropriate atomic composition on the surface of the electrode. Such synergistic effects had also been previously observed in Ni-Co alloys for hydrogen evolution, which were found to be superior to pure Ni or pure Co catalysts.[46]

Our hypothesis was also supported by electrochemical impedance spectroscopy (EIS) measurements, which further unveiled the main differences in the electrochemical properties of the mono and bimetallic catalysts. The Nyquist plots for the Co_9S_8-Ni_xS_y/Nif and Ni_3S_2/Nif are reported in Fig. S12 and were fitted using a Randles circuit, consisting of a series resistance (R_s), a charge transfer resistance (R_{ct}) and a constant phase element (CPE). The R_{ct} gives a measure of the ease of electron transfer at the electrode/electrolyte interface[11]. As reported in Tab. 1, this value is lower for the Co_9S_8-Ni_xS_y/Nif compared to Ni_3S_2/Nif, although this is not true for the less active Co_9S_8-Ni_xS_y/Nif(500,90) sample, having a similar value to the monometallic system. Another relevant parameter is the double-layer capacitance (C_{dl}), which is derived from the CPE data. The C_{dl} is an important figure of merit since it gives an estimate of the electrochemically active surface area (ECSA).[47] The calculated C_{dl} of the active Co_9S_8-Ni_xS_y/Nif elctrodes is much higher than the Ni_3S_2/Nif (Table 1), with values ranging from 44 to 64 mF/cm^2, in agreement with their superior HER activity. Again, the C_{dl} of the poorly active Co_9S_8-Ni_xS_y/Nif(500,90) sample is significantly lower and comparable to the monometallic Ni_3S_2/Nif. The enhanced electrochemically active area of the Co_9S_8-Ni_xS_y/Nif electrodes synthesized under appropriate conditions is a direct evidence of the existence of more active sites, which are linked to the particular compositional and electronic configuration at the surface. Also, the intrinsic metallic nature of the Co_9S_8 and Ni_3S_2 phases favours the rapid electron transfer at the electrode/electroyte interface.

In our discussion we treat Ni_3S_2 as the only active nickel sulfide phase in the system, without taking into account the possible effect of other phases. However this can be justified by two main observations: i) XRD, SAED and XPS gave evidence of a predominant presence of the Ni_3S_2 and $Ni_{17}S_{18}$ phases; ii) XRD analysis after the stability test evidenced the disappearence of the $Ni_{17}S_{18}$ phase (Fig.

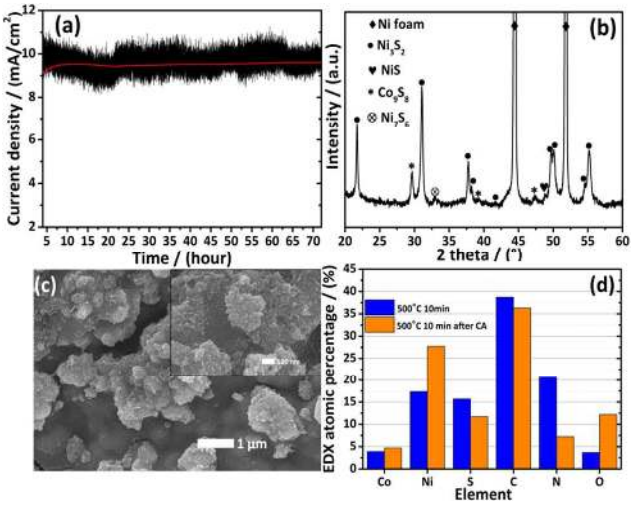

Fig. 5 (a) Chronoamperometry test for Co_9S_8-Ni_xS_y/Nif annealed at 500°C 10 min at -0.161 V vs RHE in 1M KOH. (b) XRD spectrum, (c) Low- and high magnification SEM, (d) EDX chart of Co_9S_8-Ni_xS_y/Nif after 72 hours of stability test.

View Article Online
DOI: 10.1039/C6TA00540C

5(b)), despite the fact that no current decay was observed after 72 hours for the most active sample (Co_9S_8-Ni_xS_y/Nif(500,10)), as shown in Fig. 5(a). This leads to the conclusion that the active sites are due to the biphasic Co_9S_8-Ni_3S_2 system, which is also perfectly retained after chronoamperometric test as shown by XRD, resulting in a stable and constant current density throughout the experiment. Furthermore, the Co2p and Ni2p XPS patterns reported in Fig. S10 match those of the as-synthesized sample, with a similar Co/Ni superficial atomic ratio calculated from the fitting of the XPS spectra (Table S2). The nanoparticulate morphology of the Co_9S_8-Ni_xS_y/Nif(500,10) is retained after long-term stability, as shown by the low- and high magnification SEM images in Fig. 5 (c). Only minor modifications occurred, most likely due to the dissolution of the unstable $Ni_{17}S_{18}$ phase. No cobalt leaching was observed as probed by EDX technique and summarized in the chart reported in Fig. 5 (d), with a value consistent with the as-synthesized sample.

Conclusions

We have developed a novel and facile synthetic method for the fabrication of bimetallic Co_9S_8-Ni_xS_y and monometallic Ni_3S_2 nanoparticles supported onto a 3D Ni foam. The method is based on the thermal decomposition of pre-adsorbed molecular precursors onto the metallic Ni foam, generating *in situ* the nanoparticulate metal sulfides. The bimetallic Co_9S_8-Ni_xS_y/Nif electrodes showed a significant higher activity compared to the monometallic Ni_3S_2/Nif for the hydrogen evolution reaction, with the Co_9S_8-Ni_xS_y/Nif(500,10) sample requiring a small overpotential of 163 mV at a current density of 10 mA cm^{-2} in 1M KOH electrolyte. Synthetic parameters such as annealing temperature and time were found to play a crucial role in the HER activity, establishing a stucture-property correlation through a detailed characterization analysis. The origin of the high activity of the Co_9S_8-Ni_xS_y/Nif synthesized under well-defined conditions was attributed to the existence of a synergistic effect between Co_9S_8 and Ni_3S_2 nanoparticles. This effect arises from an optimal atomic composition at the surface and an intimate contact bewteen the two nanoparticulate phases, having a small size of 20 nm. The analysis of the Tafel slopes for the active Co_9S_8-Ni_xS_y/Nif reveal a mixed Heyrovsky-Volmer mechanism occurring during the HER. It has been shown that the adsorption of reacting water molecules on the active sites is largely favoured by the Ni_3S_2 phase. The HER trend was also correlated to the electrochemical properties of the electrodes such as double layer capacitance and charge transfer resistance. Consistent results were found, with the active bimetallic Co_9S_8-Ni_xS_y/Nif samples having the largest ECSA and smallest R_{ct}. The most active Co_9S_8-Ni_xS_y/Nif(500,10) electrode was subject to chronoamperometry test, and great long-term stability was observed, with a constant current density maintained over 72 hours of reaction. The Co_9S_8 and Ni_3S_2 phases were perfectly retained after the test, as evidenced by XRD, SEM, XPS and EDX analyses. Only small morphological and structural modifications were recored as a result of the dissolution of the unstable $Ni_{17}S_{18}$ phase. Our new synthetic approach can be easily generalized and extended to the design of others 3D composite materials holding novel and unprecedented properties in a broad variety of applications such as HER/OER catalysts, supercapacitors and batteries.

Acknowledgements

This work was financially supported by the Institute of Materials Research and Engineering (IMRE), A*STAR, through funding from the core project IMRE/13-1C0102. D.A. thanks the University of Southampton for a VC scholarship and A*STAR, Singapore for funding under the ARAP award scheme. We would like to thank Dr. Hong Liu for performing Raman measurements.

Notes and references

1 P. Gerland, A. E. Raftery, H. Ševčíková, N. Li, D. Gu, T. Spoorenberg, L. Alkema, B. K. Fosdick, J. Chunn, N. Lalic, G. Bay, T. Buettner, G. K. Heilig and J. Wilmot, *Science*, 2014, **346**, 234–237.

2 Y. Tian and C. Y. Zhao, *Appl. Energy*, 2013, **104**, 538–553.

3 T. L. Gibson and N. A. Kelly, *J. Power Sources*, 2010, **195**, 3928–3932.

4 J. Luo, I. Jeong-Hyeok, M. T. Mayer, M. Schreier, M. K. Nazeeruddfn, P. Nam-Gyu, D. S. Tilley, F. Hong Jin and M. Grätzel, *Science*, 2014, **345**, 1593–1596.

5 S. A. Bonke, M. Wiechen, D. R. MacFarlane and L. Spiccia, *Energy Environ. Sci.*, 2015, **8**, 2791–2796.

6 J. a Turner, *Science*, 2004, **305**, 972–974.

7 Q. Lu, G. S. Hutchings, W. Yu, Y. Zhou, R. V Forest, R. Tao, J. Rosen, B. T. Yonemoto, Z. Cao, H. Zheng, J. Q. Xiao, F. Jiao and J. G. Chen, *Nat. Commun.*, 2015, **6**, 6567.

8 H. Zhang, Y. Li, G. Zhang, T. Xu, P. Wan and X. Sun, *J. Mater. Chem. A*, 2015, **3**, 6306–6310.

9 D. Kong, J. J. Cha, H. Wang, H. R. Lee and Y. Cui, *Energy Environ. Sci.*, 2013, **6**, 3553–3558.

10 M. S. Faber, R. Dziedzic, M. A. Lukowski, N. S. Kaiser, Q. Ding and S. Jin, *J. Am. Chem. Soc.*, 2014, **136**, 10053–10061.

11 S. Peng, N. Li, X. Han, W. Sun, M. Srinivasan, S. G. Mhaisalkar, F. Cheng, Q. Yan, J. Chen and S. Ramakrishna, *Angew. Chemie - Int. Ed.*, 2014, **53**, 12594–12599.

12 N. Jiang, L. Bogoev, M. Popova, S. Gul, J. Yano and Y. Sun, *J. Mater. Chem. A*, 2014, **2**, 19407–19414.

13 A. I. Carim, F. H. Saadi, M. P. Soriaga and N. S. Lewis, *J. Mater. Chem. A*, 2014, **2**, 13835.

14 T. F. Jaramillo, K. P. Jørgensen, J. Bonde, J. H. Nielsen, S. Horch and I. Chorkendorff, *Science*, 2007, **317**, 100–102.

15 Y. H. Chang, C. Te Lin, T. Y. Chen, C. L. Hsu, Y. H. Lee, W. Zhang, K. H. Wei and L. J. Li, *Adv. Mater.*, 2013, **25**, 756–760.

16 L. Cheng, W. Huang, Q. Gong, C. Liu, Z. Liu, Y. Li and H. Dai, *Angew. Chemie - Int. Ed.*, 2014, **53**, 7860–7863.

17 M. a Lukowski, A. S. Daniel, C. R. English, F. Meng, A. Forticaux, R. J. Hamers and S. Jin, *Energy Environ. Sci.*, 2014, **7**, 2608–2613.

18 Y. Li, H. Wang, L. Xie, Y. Liang, G. Hong and H. Dai, *J. Am. Chem. Soc.*, 2011, **133**, 7296–7299.

19 W. F. Chen, K. Sasaki, C. Ma, A. I. Frenkel, N. Marinkovic, J.

View Article Online
DOI: 10.1039/C6TA00540C

T. Muckerman, Y. Zhu and R. R. Adzic, *Angew. Chemie - Int. Ed.*, 2012, **51**, 6131–6135.
20 N. Jiang, B. You, M. Sheng and Y. Sun, *Angew. Chemie - Int. Ed.*, 2015, **54**, 6251–6254.
21 J. Tian, Q. Liu, A. M. Asiri and X. Sun, *J. Am. Chem. Soc.*, 2014, **136**, 7587−7590.
22 X. Wang, Y. V. Kolen'Ko, X. Q. Bao, K. Kovnir and L. Liu, *Angew. Chemie - Int. Ed.*, 2015, **54**, 8188–8192.
23 P. Xiao, M. Alam Sk, L. Thia, X. Ge, R. J. Lim, J.-Y. Wang, K. H. Lim and X. Wang, *Energy Environ. Sci.*, 2014, **7**, 2624–2629.
24 W.-F. Chen, C.-H. Wang, K. Sasaki, N. Marinkovic, W. Xu, J. T. Muckerman, Y. Zhu and R. R. Adzic, *Energy Environ. Sci.*, 2013, **6**, 943–951.
25 F. Harnisch, G. Sievers and U. Schröder, *Appl. Catal. B Environ.*, 2009, **89**, 455–458.
26 H. Vrubel and X. Hu, *Angew. Chemie - Int. Ed.*, 2012, **51**, 12703–12706.
27 Y. Wang, G. Zhang, W. Xu, P. Wan, Z. Lu, Y. Li and X. Sun, *ChemElectroChem*, 2014, **1**, 1138–1144.
28 M. S. Faber, M. a Lukowski, Q. Ding, N. S. Kaiser and S. Jin, *J. Phys. Chem. C*, 2014, **118**, 21347–21356.
29 L.-L. Feng, M. Fan, Y. Wu, Y. Liu, G.-D. Li, H. Chen, W. Chen, D. Wang and X. Zou, *J. Mater. Chem. A*, 2016.
30 L. L. Feng, G. D. Li, Y. Liu, Y. Wu, H. Chen, Y. Wang, Y. C. Zou, D. Wang and X. Zou, *ACS Appl. Mater. Interfaces*, 2015, **7**, 980–988.
31 X. Wu, B. Yang, Z. Li, L. Lei and X. Zhang, *RSC Adv.*, 2015, **5**, 32976–32982.
32 C. Tang, Z. Pu, Q. Liu, A. M. Asiri, Y. Luo and X. Sun, *Int. J. Hydrogen Energy*, 2015, **40**, 4727–4732.
33 Y. Sun, C. Liu, D. C. Grauer, J. Yano, J. R. Long, P. Yang and C. J. Chang, *J. Am. Chem. Soc.*, 2013, **135**, 17699–17702.
34 D. Pletcher and X. Li, *Int. J. Hydrogen Energy*, 2011, **36**, 15089–15104.
35 K. Xiong, L. Li, L. Zhang, W. Ding, L. Peng, Y. Wang, S. Chen, S. Tan and Z. Wei, *J. Mater. Chem. A*, 2015, **3**, 1863–1867.
36 C. Tang, N. Cheng, Z. Pu, W. Xing and X. Sun, *Angew. Chemie - Int. Ed.*, 2015, **54**, 9351–9355.
37 P. Ganesan, M. Prabu, J. Sanetuntikul and S. Shanmugam, *ACS Catal.*, 2015, **5**, 3625–3637.
38 N. Kumar, N. Raman and A. Sundaresan, *Zeitschrift fur Anorg. und Allg. Chemie*, 2014, **640**, 1069–1074.
39 P. Yin, L. Sun, Y. Gao and S. Wang, *Bull. Mater. Sci.*, 2008, **31**, 593–596.
40 Z. Cheng, H. Abernathy and M. Liu, *J. Phys. Chem. C Lett.*, 2007, **111**, 17997–18000.
41 N. E. Braml, A. Sattler and W. Schnick, *Chem. - A Eur. J.*, 2012, **18**, 1811–1819.
42 W. Zhou, X.-J. Wu, X. Cao, X. Huang, C. Tan, J. Tian, H. Liu, J. Wang and H. Zhang, *Energy Environ. Sci.*, 2013, **6**, 2921.
43 A. N. Buckley and R. Woods, *J. Appl. Electrochem.*, 1991, **21**, 575–582.
44 D. L. Legrand, H. W. Nesbitt and G. M. Bancroft, *Am. Mineral.*, 1998, **83**, 1256–1265.
45 J. D. Benck, T. R. Hellstern, J. Kibsgaard, P. Chakthranont and T. F. Jaramillo, *ACS Catal.*, 2014, **4**, 3957–3971.
46 C. Lupi, A. Dell'Era and M. Pasquali, *Int. J. Hydrogen Energy*, 2009, **34**, 2101–2106.
47 C. C. L. McCrory, S. Jung, J. C. Peters and T. F. Jaramillo, *J. Am. Chem. Soc.*, 2013, **135**, 16977–16987.

View Article Online
DOI: 10.1039/C6TA00540C

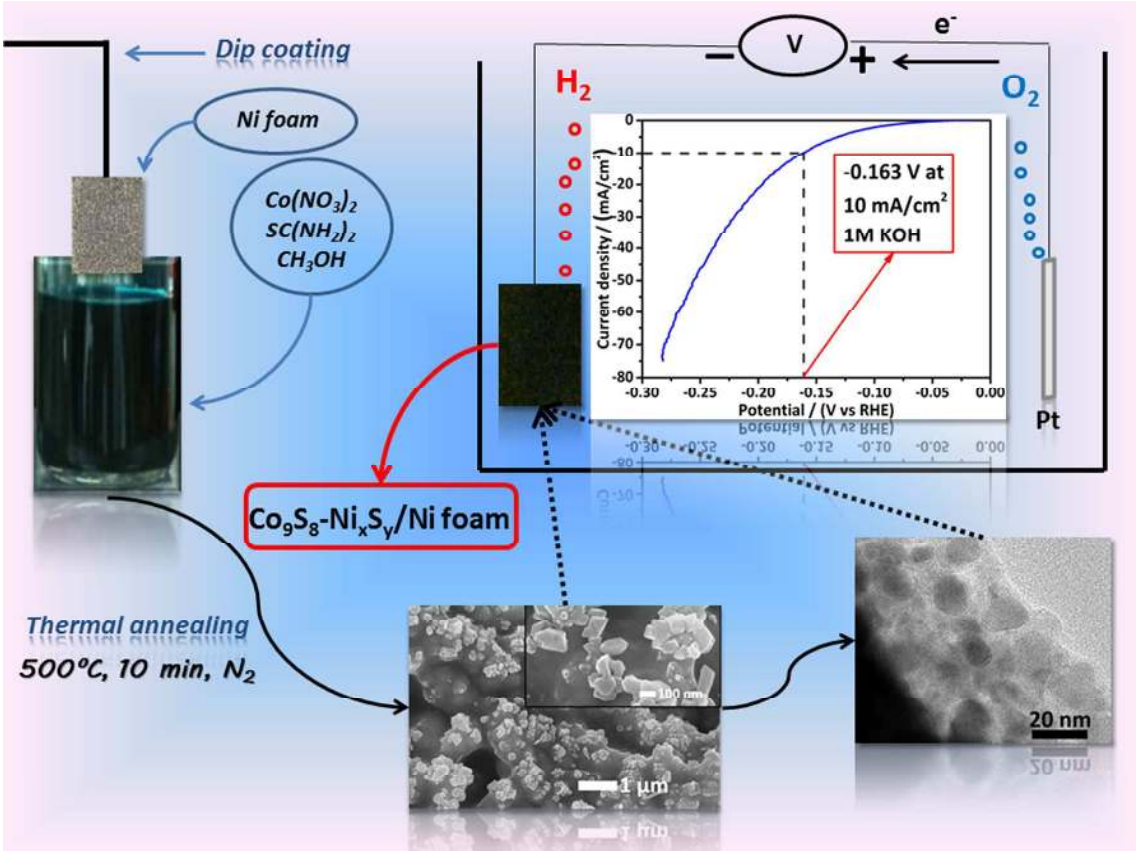

Cobalt-nickel sulfide composite electrode synthesized onto Ni foam through a facile thermal decomposition method showed remarkable activity towards electrocatalytic hydrogen production